

Electron energy distributions and electron impact source functions in Ar/N₂ inductively coupled plasmas using pulsed power

Michael D. Logue^{a)} and Mark J. Kushner^{b)}

Department of Electrical Engineering and Computer Science, University of Michigan, 1301 Beal Ave., Ann Arbor, Michigan 48109-2122, USA

(Received 6 October 2014; accepted 11 December 2014; published online 22 January 2015)

In plasma materials processing, such as plasma etching, control of the time-averaged electron energy distributions (EEDs) in the plasma allows for control of the time-averaged electron impact source functions of reactive species in the plasma and their fluxes to surfaces. One potential method for refining the control of EEDs is through the use of pulsed power. Inductively coupled plasmas (ICPs) are attractive for using pulsed power in this manner because the EEDs are dominantly controlled by the ICP power as opposed to the bias power applied to the substrate. In this paper, we discuss results from a computational investigation of EEDs and electron impact source functions in low pressure (5–50 mTorr) ICPs sustained in Ar/N₂ for various duty cycles. We find there is an ability to control EEDs, and thus source functions, by pulsing the ICP power, with the greatest variability of the EEDs located within the skin depth of the electromagnetic field. The transit time of hot electrons produced in the skin depth at the onset of pulse power produces a delay in the response of the EEDs as a function of distance from the coils. The choice of ICP pressure has a large impact on the dynamics of the EEDs, whereas duty cycle has a small influence on time-averaged EEDs and source functions. © 2015 AIP Publishing LLC.

[<http://dx.doi.org/10.1063/1.4904935>]

I. INTRODUCTION

Optimization of plasma materials processing ultimately requires control of the flux of reactive species (radicals, ions, photons) to surfaces. Control of these species is greatly facilitated by controlling the source functions resulting from electron collisions with feedstock gases and their dissociation products. This control is a direct consequence of controlling the electron energy distribution (EED).^{1–3} In steady state or continuous wave (cw) plasmas, such as low pressure inductively coupled plasmas (ICPs), the rate of ionization as determined by the EED and gas mole fractions must exactly balance the rate of loss of charged particles, either in real-time or averaged over relatively short radio-frequency (rf) cycles. (Short in this case, refers to the rf period being much smaller than the diffusion or attachment time for loss of electrons, or the time for electron energy loss.) For a given gas mixture, flow rate, power deposition, frequency, and geometry, there is usually a single EED that will provide this balance between electron sources and losses. (EEDs are, in fact, spatially varying in the plasma—in this context, we refer to the spatial average.)

Pulsed plasmas provide a means to broaden the parameter space available to customize EEDs.^{2,4} In a pulsed plasma, the power is applied over a fraction (the duty cycle, DC) of a repetitively pulsed cycle (occurring at pulse repetition frequency or PRF). In pulsed plasmas, the balance between sources and losses need only be maintained over the pulsed period which is long compared to the rf period. That is,

electron sources and electron losses can dominate at different times during the pulse period. This variability can provide additional parameters to optimize the EED, such as DC and PRF. The pulsed period can be commensurate to or longer than the time for electron loss by diffusion, attachment, or energy loss. Several studies have investigated the effect of pulsed power on plasma and radical formation in electron cyclotron resonance (ECR) plasmas^{5–7} and ICPs.^{8–10} Low pressure ICPs are particularly attractive for control of EEDs through pulsing. In these systems, ionization processes are dominated by the inductively coupled power. There is a smaller contribution to ionization by surface associated processes, such as secondary electron emission and acceleration of secondary electrons by sheaths in ICPs compared to capacitively coupled plasmas (CCPs). This enables a more direct correlation between ICP power deposition and electron heating. Substrate biases for ion acceleration applied to ICPs operating in a high plasma density mode have little effect on the EEDs due to the small amount of electron heating produced by the thin sheaths.

Kortshagen *et al.* measured the spatial variation of electron energy probability functions (EPPFs) in an argon ICP under cw conditions at pressures of 5–40 mTorr.¹¹ (Note that EEDs are normalized to unity when integrating over energy. EPPFs are normalized to the total electron density when integrating over energy.) They compared the EPPFs to theoretical results from a 1D model. They found that with increasing pressure, there was a change in the shape of the EPPF from concave to convex in the elastic energy range ($\varepsilon < 11.6$ eV) and that the EPPFs displayed non-local behavior. Singh and Graves measured EPPFs in cw ICPs sustained in Ar, N₂, Ar/N₂, and other gases.¹² In Ar, they found that varying

^{a)}mdlogue@umich.edu

^{b)}Author to whom correspondence should be addressed. Electronic mail: mjkkush@umich.edu

power while keeping pressure constant at 10 mTorr had little effect on the EEPFs. When keeping the power constant at 300 W and varying pressure from 2–40 mTorr, they found the EEPFs to be non-Maxwellian at all pressures, although for 10–40 mTorr, the EEPFs were nearly Maxwellian below the inelastic collision thresholds. The EEPFs were two-temperature distributions above 10 mTorr and three-temperature distributions at 2 mTorr. In ICPs sustained in N_2 at 450 W, a decrease in the EEPFs near 3 eV occurred as the pressure was increased from 10 to 100 mTorr due to the increased importance of energy loss resulting from vibrational excitation. In Ar/ N_2 discharges, increasing the Ar fraction reduced this decrease in the EEPF and reduced the propensity for two-temperature distributions.

Malyshev and Donnelly investigated the temporal dynamics of electron temperature (T_e), electron density (n_e), and the EEPF in a pulsed ICP sustained in Cl_2 with an rf substrate bias.¹³ They found that during the afterglow of the power pulse, the rf bias on the substrate did affect the EEPFs. As the plasma density decreased during the afterglow due to diffusion and attachment, the sheath thickness at the substrate increased. The widening sheath increased the rate of stochastic electron heating which then increased the rate of heating of the EEPF. When the ion density decayed to values normally associated with CCPs, the EEPFs became indistinguishable from those of cw reactive ion etching (RIE) plasmas.

Hebner and Fleddermann investigated the effect of peak rf power, duty cycle, and PRF on electron density and plasma potential in pulsed ICPs sustained in Ar and Cl_2 .¹⁴ They found that the peak electron density initially increased with duty cycle before decreasing above 30%. This is due to a balance between the amount of power being deposited into the plasma and the time it takes for the n_e source and loss mechanisms to come into equilibrium. Increasing rf power led to larger peak values of n_e , while increasing PRF caused n_e to decay to lower values in the plasma afterglow. This produced a greater dynamic range in n_e during the pulse. Increased duty cycle was also found to cause the peak plasma potential to decrease due to a higher residual n_e at the beginning of the pulse shielding the bulk plasma from the applied rf potential.

Kimura and Ohe investigated the effect of pressure on the EEPFs in Ar discharges in a planar ICP system.¹⁵ They found that for a cw power of 50 W, the EEPF had a three-temperature distribution at 5 mTorr due to the depletion of high-energy electrons at inelastic thresholds.¹⁵ The EEPF had a bi-Maxwellian structure below the first inelastic threshold. The EEPFs at pressures higher than 10 mTorr were two-temperature distributions. The slope of the tail of the EEPF is dominated by inelastic collisions as opposed to electron-electron collisions, which results in the EEPF having two temperatures for the bulk and tail of the EEPF. Maresca *et al.* experimentally investigated the cooling of electrons and EEPFs in a planar, pulsed Ar ICP.¹⁶ They attributed observed decays in the tail of the EEPFs to both inelastic collisions and to loss of electrons having energy greater than the sheath potential to walls, a process often called diffusion cooling.

Godyak *et al.* investigated the effect of power, pressure, and rf frequency on EEPFs and plasma parameters in an Ar ICP.¹⁷ At 100 mTorr, the plasma is collisionally dominated and the EEPF at all powers appears almost Maxwellian in the elastic energy range and is depleted above the inelastic energy threshold (≈ 11.6 eV). This EEPF appears as a two-temperature distribution. At 10 mTorr, a three-temperature structure is observed for the EEPF at low power which transitions to a two-temperature distribution with increasing power. At lower pressure, 1–10 mTorr, the rf frequency had a noticeable effect on the EEPF at all powers, with reduced electron heating at higher frequencies due to the reduced skin depth of the electromagnetic field.

Godyak investigated non-equilibrium EEPFs in ICPs and discussed ways to control electron temperatures, T_e , and thus EEPFs.¹⁸ He found that there may be a two-temperature distribution in the EEPF due to anomalous skin effects, where the rf current is not a local function of the rf field. One such effect is selective, collisionless heating of the faster and hotter electrons that cross the sheath in a fraction of the rf period—the selective nature of this heating can lead to two-temperature distributions. In low pressure ICPs having an anomalous skin effect, the effective electron temperature was found to have a strong dependence on frequency. This frequency effect is reduced as the plasma density increases and the EEPF becomes more Maxwellian due to increased electron-electron collisions.¹⁸

Another method to control T_e , and thus EEPFs, as discussed by Godyak,¹⁸ is pulsing of the discharge power, which decouples the electron heating and electron energy loss processes. During repetitive pulsing, at the beginning of the activeglow (power pulse-on time), T_e initially overshoots the steady state value of T_e , before decaying to the steady state value. This spike in T_e is due to the ICP power being dissipated into a smaller electron density than the activeglow steady state density. The T_e must also exceed the value for which ionization balances losses in order to increase the electron density during the beginning of the power pulse. The steady state value of T_e in the activeglow may be different from T_e with cw excitation even if the pulse-period-average (PPA) power is the same. During the afterglow (power pulse-off time), T_e quickly decays below the cw steady state value due to collisional energy losses and diffusion cooling. This phenomenon has a pressure dependence, as lower pressures will result in higher T_e during the pulse-on time as well as a faster cooling rate during the pulse-off time due to diffusion cooling. At lower pressures, the electron mean free path is longer, which reduces energy loss from collisions during the pulse-on time and allows higher energy electrons to more rapidly diffuse to the walls.¹⁸

In this paper, results from a computational investigation of EEDs and electron impact source functions in a pulsed Ar/ N_2 planar ICP discharge are presented. This gas mixture was chosen as there are collisional energy loss reactions at low (vibrational excitation), intermediate (electronic excitation), and high (ionization) energies. The consequences of pulsed power for various duty cycles and pressures on EEDs and source functions for $N_2(v=1)$, $N_2(A)$, and Ar^+ through direct electron-impact reactions are discussed. The threshold

energies of these processes are 1.3 eV, 6 eV, and 16 eV, which are intended to be representative of low-, mid-, and high-threshold processes, respectively.

The model used in this investigation is briefly described in Sec. II. Computed results on the effect of pulsing on plasma parameters are discussed in Sec. III. Computed results for EEDs at different heights for different operating conditions and the effect of pulsing on source functions are discussed in Sec. IV. Our concluding remarks are in Sec. V.

II. DESCRIPTION OF THE MODEL

The model employed in this investigation is the Hybrid Plasma Equipment Model (HPEM), described in detail in Ref. 19. The HPEM is a two-dimensional model consisting of separate modules, each of which addresses different physical phenomena. Information is transferred between modules in a hierarchical manner. The modules are executed sequentially on time scales short enough to resolve pulsed periods. The modules used in this investigation are the following. The Electromagnetics Module (EMM) is used to solve Maxwell's equations for antenna produced electric and magnetic fields. Using cylindrical coordinates and antenna currents in the azimuthal direction, the EMM produces $E_\theta(\vec{r}, \phi)$, $B_r(\vec{r}, \phi)$, and $B_z(\vec{r}, \phi)$, where ϕ is the spatially dependent phase. The Electron Energy Transport Module (EETM) uses these fields from the EMM and electrostatic electric fields ($E_r(\vec{r}, \phi)$, $E_z(\vec{r}, \phi)$) from the Fluid Kinetics-Poisson Module (FKPM) to produce EEDs which in turn produce electron transport and impact rate coefficients. This is accomplished by using an electron Monte Carlo simulation (eMCS), including electron-electron collisions. The eMCS is discussed in detail in Ref. 20. The FKPM is used to obtain densities, fluxes, and temperatures of all charged and neutral species, as well as the electric potential from the solution of Poisson's equation. Separate continuity, momentum, and energy equations are used for all heavy species. Continuity equations are used for electrons, where fluxes are determined using a drift-diffusion method. The electron temperature discussed below is obtained from $T_e = 2/3\langle\epsilon\rangle$, where the average electron energy $\langle\epsilon\rangle$ is computed from the electron energy distributions produced by the EETM.

The typical sequence of events to model pulsed ICPs is the following. A pulse power waveform, usually power as a function of time, is specified. The HPEM is then executed with cw excitation with the PPA power using acceleration techniques until a quasi-steady state is achieved. All acceleration is then turned off and the pulse cycle is then started. A sufficient number of pulsed cycles (typically 6–7) is then executed to achieve a pulse-periodic steady state.

All results are for plasmas sustained in $\text{Ar}/\text{N}_2 = 80/20$ mixtures. The species consist of Ar (ground state); Ar^* , Ar^{**} , Ar^{***} , Ar^+ , N_2 (ground state); $\text{N}_2(v)$, N_2^* , N_2^+ , N (ground state); N^* , N^+ , and electrons. Ar^* represents the combined metastable states of the $\text{Ar}(3p^54s)$ manifold [$\text{Ar}(1s_5)$, $\text{Ar}(1s_3)$] and Ar^{**} represents the combined radiative states [$\text{Ar}(1s_4)$, $\text{Ar}(1s_2)$]. Ar^{***} is a lumped state representing $\text{Ar}(3p^54p)$ and higher states. Radiation trapping of the Ar^{**} state is included. $\text{N}_2(v)$ represents the combined

vibrational states of N_2 , and N_2^* represents the combined electronic states of N_2 . N^* represents the combined electronic states of atomic nitrogen, $\text{N}(4s^22d)$ and $\text{N}(4s^22p)$.

A schematic of the ICP reactor used in the computational investigation is shown in Fig. 1. The plasma is sustained in a 25 cm diameter reactor, 16.5 cm tall with a three-turn planar coil on top of a dielectric window. Gas is injected through a cylindrical nozzle at the top underneath the center coil of the ICP and pumped annularly at the bottom. Computed plasma parameters [electron temperature (T_e), electron density (n_e), and electron impact source function (S_e)], EEDs, and source functions for $\text{N}_2(v=1)$, $\text{N}_2(A)$, and Ar^+ are discussed below. EEDs and source functions will be compared between heights of 11.5 cm and 5.5 cm, inside and outside the electromagnetic skin depth, respectively. In all cases, the PPA power is 300 W, the PRF is 20 kHz, the ICP frequency is 10 MHz, and the gas flow rate is 100 sccm.

III. EFFECT OF PULSED POWER ON PLASMA PARAMETERS

Plasma parameters during a pulse period of the ICP power are first discussed for a duty cycle of 30% and pressure of 5 mTorr. The spatial profiles for n_e , T_e , and net electron impact ionization source, S_e , for different times during the pulse period are shown in Figs. 2–4. T_e at a radius of 5.9 cm and heights of 11.5 cm (in the skin depth) and 5.5 cm (below the midplane) as a function of time for different pressures is shown in Fig. 5. n_e for the same conditions is shown in Fig. 6. The densities of $\text{N}_2(v=1)$, $\text{N}_2(A)$, Ar^+ , and n_e at a radius of 5.9 cm and heights of 11.5 cm and 5.5 cm as a function of time for a pressure of 5 mTorr are shown in Fig. 7.

At the start of the power-on period, n_e , T_e , and S_e first increase near the coil underneath the nozzle. The ICP power is deposited within the skin depth of the rf field ($\approx 1\text{--}2\text{ cm}$) and only those electrons located in the skin depth are initially

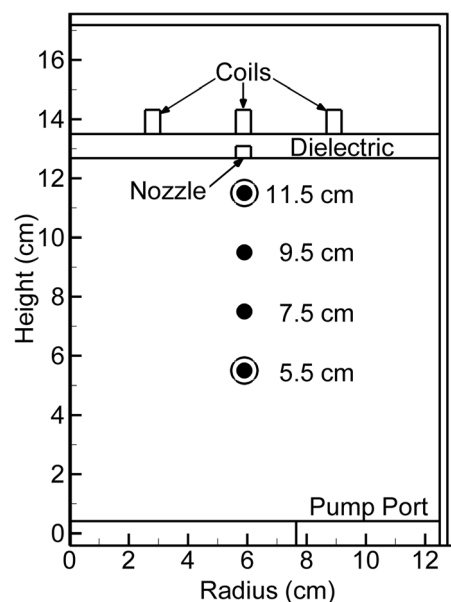


FIG. 1. Schematic of the inductively coupled plasma reactor used in the model. Plasma properties are discussed at heights of 5.5 and 11.5 cm.

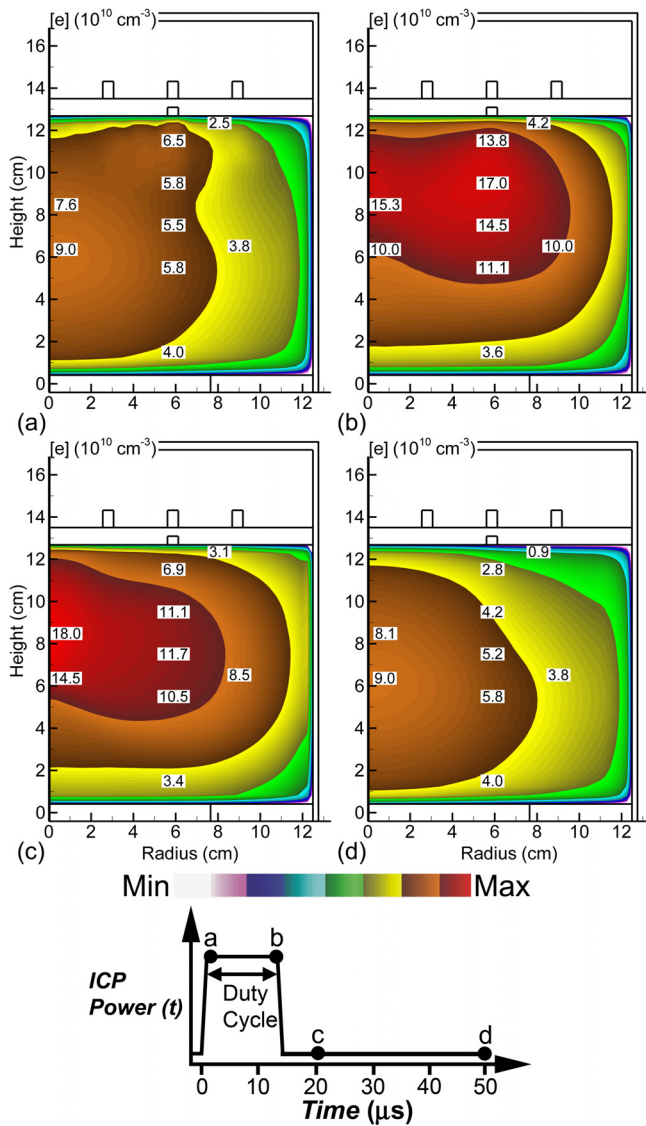


FIG. 2. Electron density at different times during a pulsed cycle of the ICP. Plasma conditions are Ar/N₂ = 80/20, 300 W pulsed-period-averaged power, 5 mTorr, 100 sccm, 10 MHz, pulse repetition frequency = 20 kHz, duty cycle = 30%. (a) Start of the pulse-on period, (b) end of pulse-on period, (c) 4 μs after start of afterglow period, and (d) end of afterglow period. These times are indicated in the schematic at the bottom of the figure.

heated. At 5 mTorr, the mean-free-path for electron energy loss is ≈20 cm, and so the skin depth is anomalous, that is partly non-collisional. With the exception of the initial spike in T_e (discussed below), T_e in the skin depth layer is 5–6 eV. These higher energy electrons then transport lower into the chamber, undergoing momentum transfer collisions and inelastic collisions producing excitation and ionization. The calculation of T_e is dominated by the far more numerous low energy electrons, while excitation and ionization are dominated by the sparse high energy electrons which also have longer mean-free-paths. As a result, S_e which is determined by higher energy electrons, appears to extend further from the skin depth than does T_e .

At 5 mTorr, there is a spike in T_e at a height of 11.5 cm, near the coils, at the start of the pulse to as high as 12.3 eV, a phenomenon typically called *overshoot*.² At the beginning of the pulse, power is dissipated into a smaller inventory of

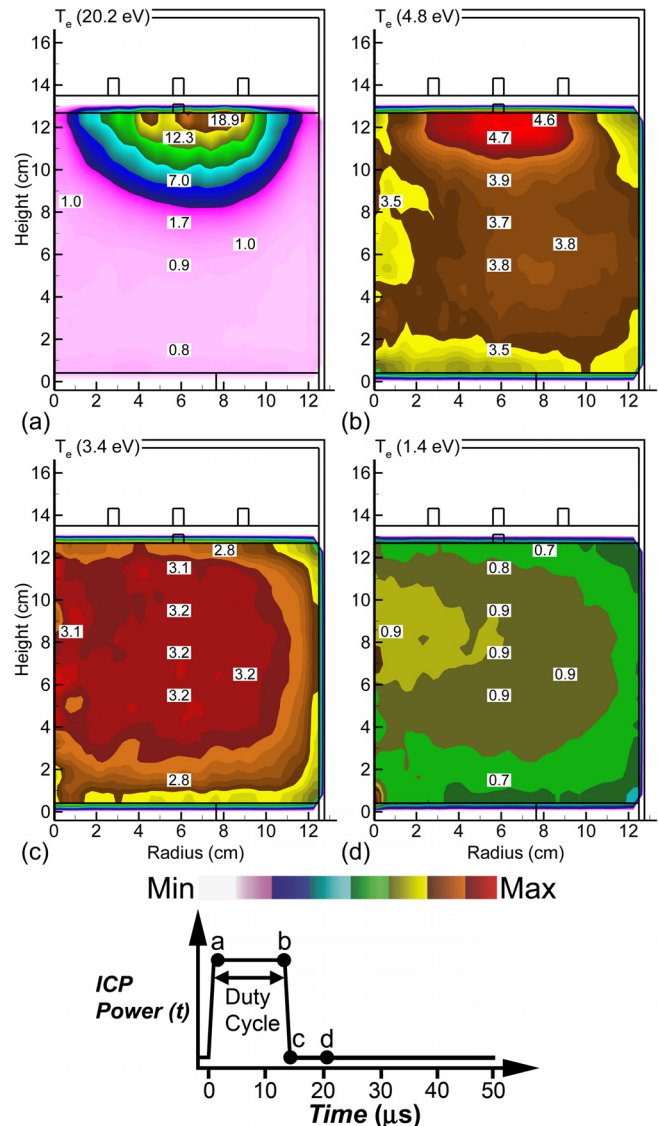


FIG. 3. Electron temperature at different times during a single pulse of the ICP. Plasma conditions are Ar/N₂ = 80/20, 300 W pulsed-period-averaged power, 5 mTorr, 100 sccm, 10 MHz, pulse repetition frequency = 20 kHz, duty cycle = 30%. (a) Start of the pulse-on period, (b) end of pulse-on period, (c) start of afterglow period, and (d) 4 μs after start of afterglow period. These times are indicated in the schematic at the bottom of the figure.

electrons, which then elevates their temperature above the quasi-steady state value, 4.5–5 eV. In fact, T_e must at some point exceed the quasi-steady state value in order to increase the plasma density from its pre-pulse value. The local spike in S_e is $8 \times 10^{16} \text{ cm}^{-3} \text{ s}^{-1}$, compared to a quasi-steady state value during the pulse of $10^{16} \text{ cm}^{-3} \text{ s}^{-1}$. The spikes in both T_e and S_e produce a local maximum in n_e under the coils of $6.5 \times 10^{10} \text{ cm}^{-3}$. The modulation in the value of n_e at a height of 11.5 cm during the pulse period is a factor of 5. The modulation in T_e is significantly greater, requiring only 5 μs to decrease to 0.5 eV when power is terminated, a value that is then sustained largely by heating from superelastic electron collisions with long lived metastable states in the afterglow. Note that S_e , in particular, peaks under the center coils, which is also where gas is injected. This peak in S_e occurs in part because the inductively coupled electric field is highest at that radius. The peak is also due to a local

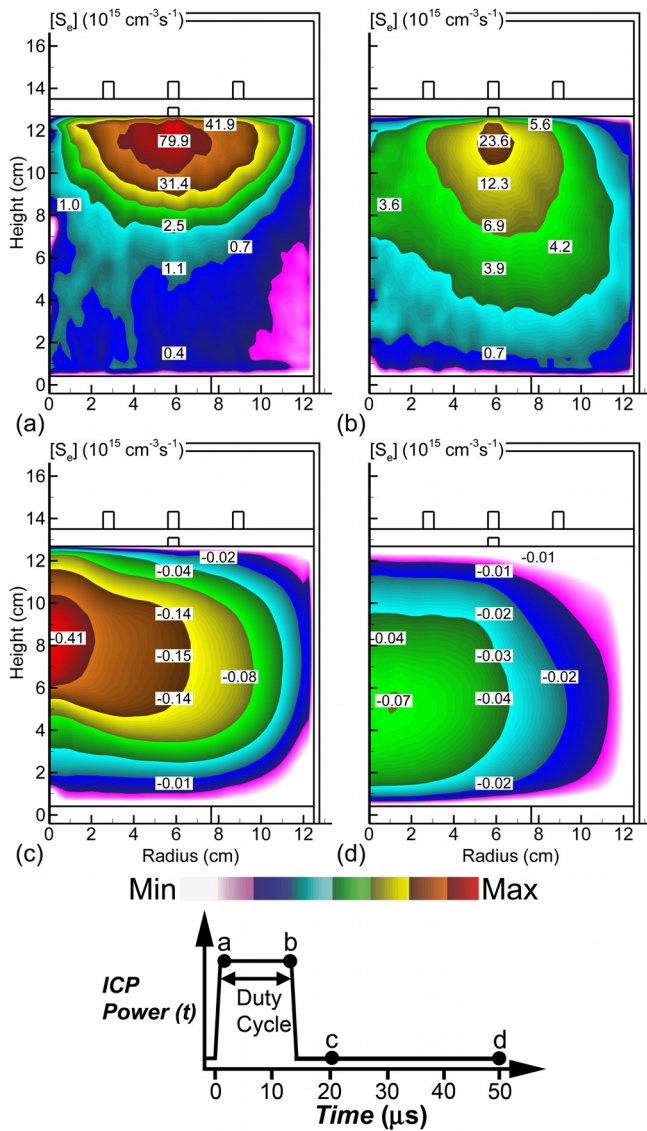


FIG. 4. Electron source function at different times during a single pulse of the ICP. Plasma conditions are Ar/N₂ = 80/20, 300 W pulsed-period-averaged power, 5 mTorr, 100 sccm, 10 MHz, pulse repetition frequency = 20 kHz, duty cycle = 30%. (a) Start of pulse-on period, (b) end of pulse-on period, (c) 4 μs after start of afterglow period, and (d) end of afterglow period. These times are indicated in the schematic at the bottom of the figure.

increase in gas density due to the jetting of the input gases in front of the nozzle which locally enables more collisions.

When the ICP power is turned off, the rapid decay in T_e leads to electron loss through diffusion to the walls and recombination being larger than electron generation through electron impact ionization. This results in S_e transitioning from positive to negative in the bulk plasma, that is, a change from a net source to a net loss. The maximum net loss is $4 \times 10^{14} \text{ cm}^{-3} \text{ s}^{-1}$, which is dominated by dissociative recombination of N_2^+ . This rate of loss in the volume during the afterglow is small compared to ionization rates during the pulse, and so electron loss is still dominated by diffusion. The rate coefficient for dissociative recombination scales as $T_e^{-0.5}$, which is not a strong temperature dependence compared to ionization. Therefore, the negative S_e resulting from recombination largely follows the plasma density during the afterglow phase of the pulse cycle. The most negative S_e

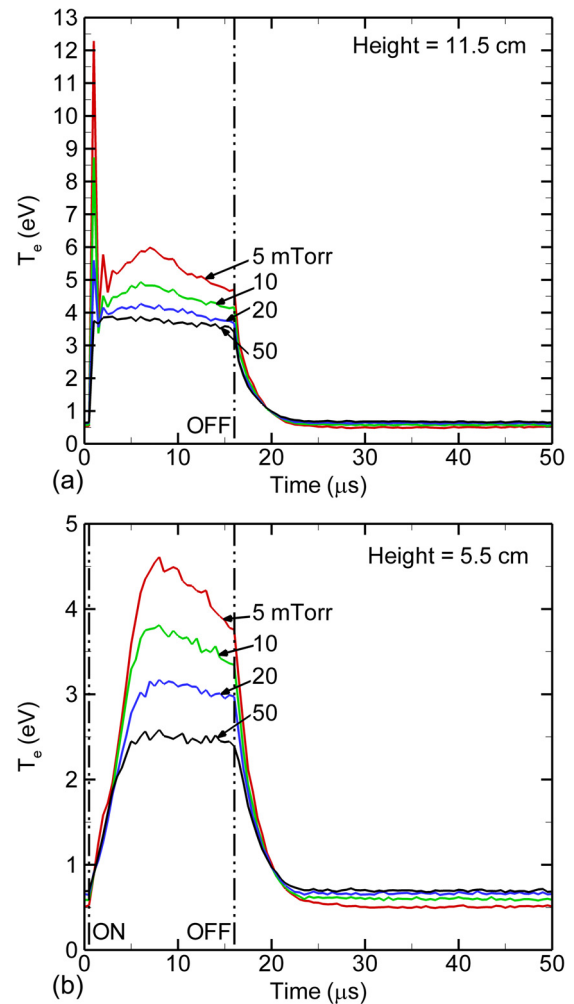


FIG. 5. Electron temperature as a function of time at a radius of 5.9 cm for a single pulse at different pressures at two positions. Plasma conditions are Ar/N₂ = 80/20, 300 W pulsed-period-averaged power, 100 sccm, 10 MHz, pulse repetition frequency = 20 kHz, duty cycle = 30%. Heights are (a) 11.5 cm and (b) 5.5 cm.

transition occurs towards the center of the reactor where the electron and ion densities are largest.

When the ICP power is turned on, there is an initial overshoot of both T_e (at all pressures), followed by a decay to a quasi-steady state value, as shown in Fig. 5. At pressures of ≤ 10 mTorr, the initial electron density is low enough that there is a large overshoot in T_e (9–12 eV) before the temperature begins to settle towards a steady state value. There is not a strong overshoot at higher pressures due to there being a smaller modulation in the electron density, as shown in Fig. 6, due to the lower rate of electron loss by diffusion during the afterglow. This lower rate of electron loss during the pulse produces the lower steady state value of T_e and longer rise time of electron density with increasing pressure. If the rate of ionization is constant, then the time to reach a steady state is determined by the rate of electron loss.

As pressure increases, the rate of collisional cooling increases while the rate of diffusion cooling decreases due to the reduction in the electron mean free path. This process is somewhat mitigated by gas heating which rarefies the gas and reduces the gas density. From 5 mTorr to 50 mTorr, the

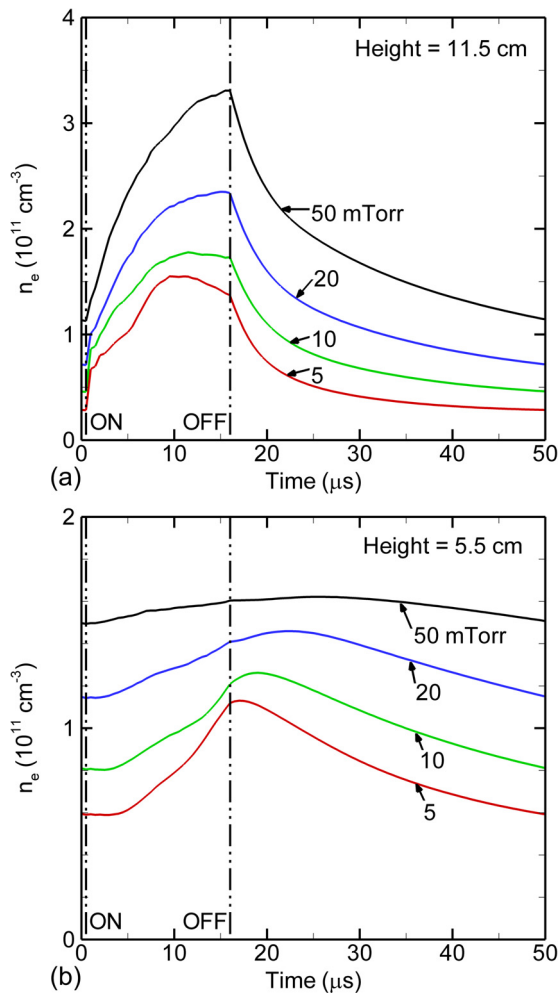


FIG. 6. Electron density as a function of time at a radius of 5.9 cm for a single pulse at different pressures at two positions. Plasma conditions are $\text{Ar}/\text{N}_2 = 80/20$, 300 W pulsed-period-averaged power, 100 sccm, 10 MHz, pulse repetition frequency = 20 kHz, duty cycle = 30%. Heights are (a) 11.5 cm and (b) 5.5 cm.

reactor averaged gas temperature increases from ≈ 550 K to ≈ 620 K. As pressure increases, the increase in collisionality as well as the higher n_e at the beginning of the pulse, suppresses oscillations in T_e .

The modulation in electron density during the pulse is greater in the skin depth (height of 11.5 cm) than lower in the reactor (5.5 cm) as shown in Fig. 6. At 50 mTorr, the modulation in electron density is a factor of nearly 3 in the skin depth ($1.2 \times 10^{11} \text{ cm}^{-3}$ to $3.4 \times 10^{11} \text{ cm}^{-3}$), whereas lower in the reactor, the electron density is $1.5 \times 10^{11} \text{ cm}^{-3}$ and has a modulation only about 5%. As the pressure increases, the skin depth becomes progressively more collisional and less anomalous. As such, the region of positive electron sources during the power pulse is progressively confined within the skin depth. Electrons then diffuse downward with transit times that are commensurate with the interpulse period. The diffusional nature of this transport then averages the periodic electron sources.

The modulation of n_e , $\text{N}_2(v=1)$, $\text{N}_2(\text{A})$, and Ar^+ during the pulsed period at a pressure of 5 mTorr is shown in Fig. 7 within the skin depth (height of 11.5 cm) and lower in the reactor (5.5 cm). The modulation of these densities is

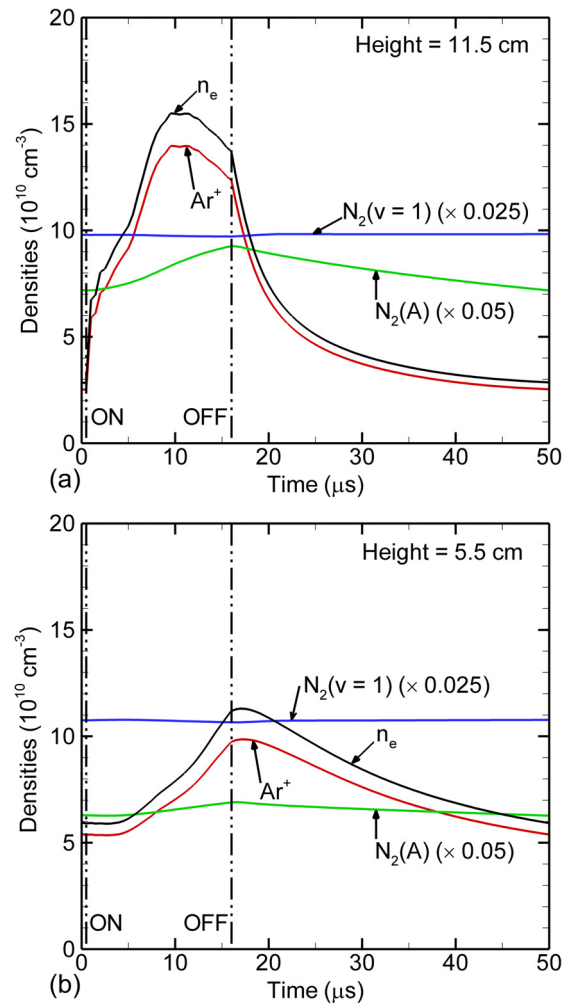


FIG. 7. Densities of plasma species (n_e , $\text{N}_2(v=1)$, $\text{N}_2(\text{A})$, and Ar^+) at a radius of 5.9 cm as a function of time for a single pulse at two positions. Plasma conditions are $\text{Ar}/\text{N}_2 = 80/20$, 300 W pulsed-period-averaged power, 5 mTorr, 100 sccm, 10 MHz, pulse repetition frequency = 20 kHz, duty cycle = 30%. Heights are (a) 11.5 cm and (b) 5.5 cm.

determined by the modulation in T_e and the threshold energies for generation of these species. As the power-on portion of the cycle begins, there is an overshoot in T_e in the skin depth that lasts a few microseconds, as shown in Fig. 5, followed by a quasi-steady T_e of 5–6 eV for the remainder of the power-on part of the cycle. The pulsing of T_e naturally preferentially increases the rate of excitation of high threshold species, such as Ar^+ , relative to lower threshold species, such as $\text{N}_2(\text{A})$ and $\text{N}_2(v=1)$. This leads to a large fractional increase in $[\text{Ar}^+]$ relative to $[\text{N}_2(\text{A})]$, and larger increase in $[\text{N}_2(\text{A})]$ relative to $[\text{N}_2(v=1)]$. The modulation in $[\text{N}_2(v=1)]$ is nominal. The amount of modulation is in part determined by the fractional change in density produced during each pulse. Ar^+ is rapidly generated during each pulse but is also rapidly lost by ambipolar diffusion, and so there is significant modulation. The rates of loss of $\text{N}_2(\text{A})$ and $\text{N}_2(v=1)$, also dominantly by diffusion, are lower and so their modulation is less significant.

At 5 mTorr and a height of 5.5 cm, which is below the midplane of the reactor, n_e and $[\text{Ar}^+]$ do not immediately increase at the start of the pulse, while the densities

immediately increase in the skin depth. There is a finite speed at which power in the form of energetic electrons capable of ionizing are transferred from the skin layer through the plasma outside the skin layer to the center of the reactor. This transport of high energy electrons lifts the tail of the EED sufficiently to initiate an increase in ionization and electron density. The speed of this downward propagating ionization wave can be estimated from Figs. 5 and 7. The overshoot in T_e in the skin depth at a height of 11.5 cm occurs at $t \approx 1 \mu\text{s}$ which coincides with the onset of the increase in n_e at that height. The maximum in T_e at a height of 5.5 cm occurs at $\approx 8 \mu\text{s}$ which is when n_e begins to significantly increase. The corresponding speed of the ionization wave is $\approx 10^6 \text{ cm}\cdot\text{s}^{-1}$.

IV. EEDs AND SOURCE FUNCTIONS DURING THE PULSE PERIOD

Pulsing of the power significantly modulates the EEDs, $f(\epsilon)$, which then determine both instantaneous and cycle averaged excitation rates. As a source of validation of our model, EEPFs for ICPs, $f_P(\epsilon)$, sustained in Ar/N₂ mixtures are compared to the experimental results of Langmuir probe measurements by Singh and Graves¹² in Fig. 8. The cw power is 350 W, pressure is 60 mTorr, and the EEPF is experimentally measured along the axis of the chamber at a height 7.6 cm below the top dielectric window. Recall that the $f_P(\epsilon)$ reflects both the electron density and $f(\epsilon)$. The implied magnitudes of the electron density from the $f_P(\epsilon)$ agree well between the experiment and model. The $f_P(\epsilon)$, resembles a Maxwellian at low N₂ content, which is captured by the model. As the N₂ fraction increases, electron energy loss due to resonant vibrational excitation of N₂ begins to deplete electrons above 2–3 eV. The results from the model show a clearer cut-off in the EEPF at high N₂ fraction than in the experiment. This discrepancy could be a result of too low contribution of electron-electron (e-e) collisions in the model, which tend to smooth the distribution towards a Maxwellian. There could also be a contribution from the well-known distortion in the experimental probe characteristics at low energy or there being capacitive coupling in the experiment that is not captured in the model. (The model results are for pure inductive coupling.)

As another source of validation of our model, EEPFs for ICPs sustained in Ar/N₂ mixtures were compared to the experimental results of Langmuir probe measurements by Kimura and Kasugai,²¹ as shown in Fig. 9. For this comparison, the dimensions and layout of the experimental reactor were reproduced in the model—inner diameter of 16 cm and height of 4 cm—with the probe measurements being made in the center of the chamber. The computed $f_P(\epsilon)$ at 60 mTorr agrees well with the experiment over the range of Ar fractions of 85% to 50% in both shape and magnitude. The exception is for the well-known distortion in the probe characteristics at energies of less than a few eV. The model under-predicts the plasma density with increasing Ar fraction (decreasing N₂ fraction) by perhaps 50% for the largest Ar fraction of 85%. The agreement at 30 mTorr, or twice the power density of 60 mTorr, is also good, particularly at low

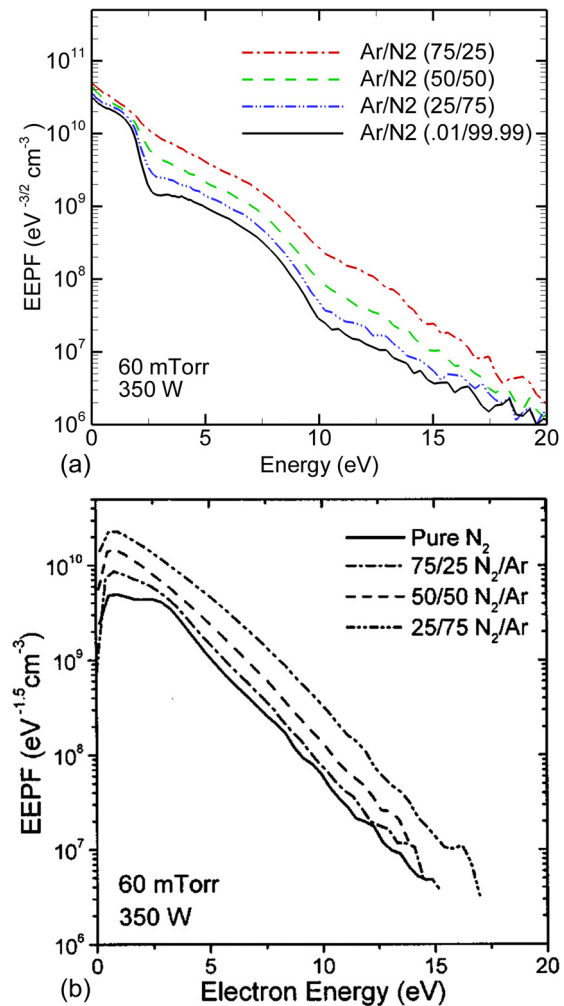


FIG. 8. EEPFs in an Ar/N₂ ICP for different gas mixtures. Comparison is made to the experimental results found in Ref. 12. (a) Simulated plasma conditions are cw, 350 W, 60 mTorr, 100 sccm, 10 MHz. (b) Experimental conditions are the same except the ICP frequency is 13.56 MHz.

Ar fraction (large N₂ fraction). Again, the model under-predicts the plasma density by about a factor of 2 at the lowest N₂ fraction.

$f(\epsilon)$ at different times during the pulse cycle, at pressures of 5, 20, and 50 mTorr for a radius of 5.9 cm and height of 11.5 cm (in the skin depth) are shown in Fig. 10; and at 5.5 cm (below the midplane) are shown in Fig. 11. The time during the pulse period for each plot is shown in the diagram at the bottom of the figures. The ICP is operated with a PPA power of 300 W and a duty cycle of 30%. The threshold energies for excitation of N₂($v=1$), N₂(A) and Ar⁺ are indicated by dashed lines. At 5 mTorr, the overshoot in T_e in the skin depth produces an extension of $f(\epsilon)$ to high energies, which persists for the duration of the power-on portion of the cycle. Upon termination of the power, $f(\epsilon)$ decays most rapidly at energies above the threshold for excitation of N₂(A) at 6.2 eV. As $f(\epsilon)$ thermalizes during the afterglow, the $f(\epsilon)$ separates into two regions. The cross sections for vibrational excitation of N₂ are resonant with appreciable values only between 1.3 and 3.8 eV. The threshold for electronic excitation of N₂(A) is at 6.2 eV. There is an energy region between

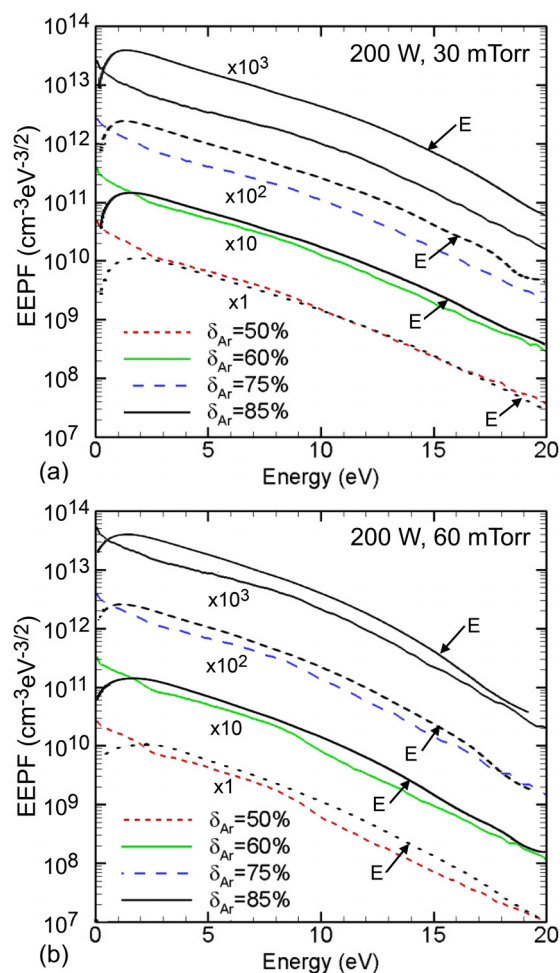


FIG. 9. EPPFs in Ar/N₂ ICPs for argon fractions of 50%–85%. Comparison is made to the experimental results of Kimura and Kasugai found in Ref. 21. Operating conditions are cw, 200 W, 20 sccm in a chamber 16 cm in diameter and 4 cm tall. The experimental results are labeled with “E.” (a) 30 mTorr and (b) 60 mTorr.

3.8 eV and 6.2 eV where elastic collisions dominate. Electrons between these two energies have a lower rate of energy loss than either lower or higher energies. For example, at the start of the afterglow at a height of 11.5 cm, the power loss per electron at 5 eV, where elastic collisions dominate, is ≈ 286 eV/s. At 2 eV, the power loss is $\approx 3.4 \times 10^5$ eV/s and at 8 eV is $\approx 2.0 \times 10^5$ eV/s. Electrons will persist in the elastic energy gap for extended periods of time due to their low power loss.

At a height of 5.5 cm and 5 mTorr, the tail of $f(\epsilon)$ rises as electrons accelerated in the skin depth transport across the reactor. The tail of $f(\epsilon)$ at time 1 (beginning of power-on) is depressed at the lower height, while the tail is already extended to high energy in the skin depth. $f(\epsilon)$ at the lower height has a two-temperature distribution early during the pulse as the less populated tail is more rapidly populated with high energy, long mean free path electrons than the more collisional low energy portion of the distribution. The tail is not fully populated until time 2 (the end of the power-on period at 12 μ s). The decay process for $f(\epsilon)$ at the lower height is nearly the same as in the skin-depth. The decay of electron energy has both local (collisional) and non-local (diffusion cooling) components, neither of which strongly

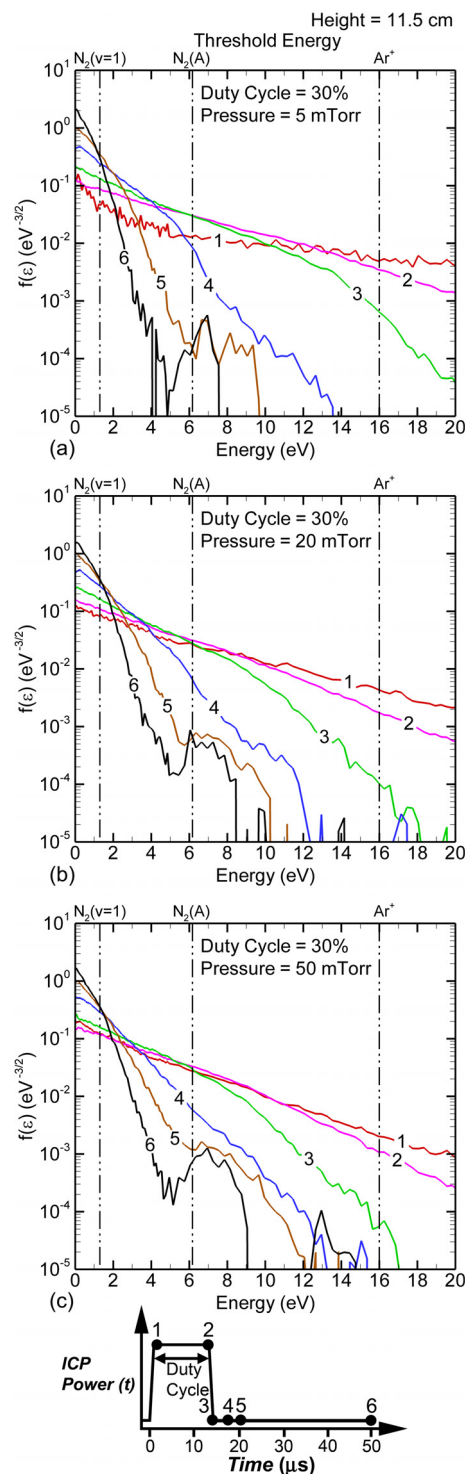


FIG. 10. $f(\epsilon)$ as a function of time during the pulse period in the skin depth at a height of 11.5 cm (Ar/N₂ = 80/20, 300 W pulsed-period-averaged power, 100 sccm, 10 MHz, PRF = 20 kHz, DC = 30%) (a) 5 mTorr. (b) 20 mTorr. (c) 50 mTorr. The threshold energies for N₂(v = 1), N₂(A), and Ar⁺ are shown by the dashed lines.

depends on position. Collisional energy loss depends only on the local density and mole fractions of the gas. Although the gas is somewhat rarefied in the center of the reactor ($T_{gas} = 632$ K) compared to near the walls, the mole fractions of different species are fairly uniform. So the rate of collisional loss is nearly the same as a function of position. The non-local component of the decay of $f(\epsilon)$, diffusion cooling,

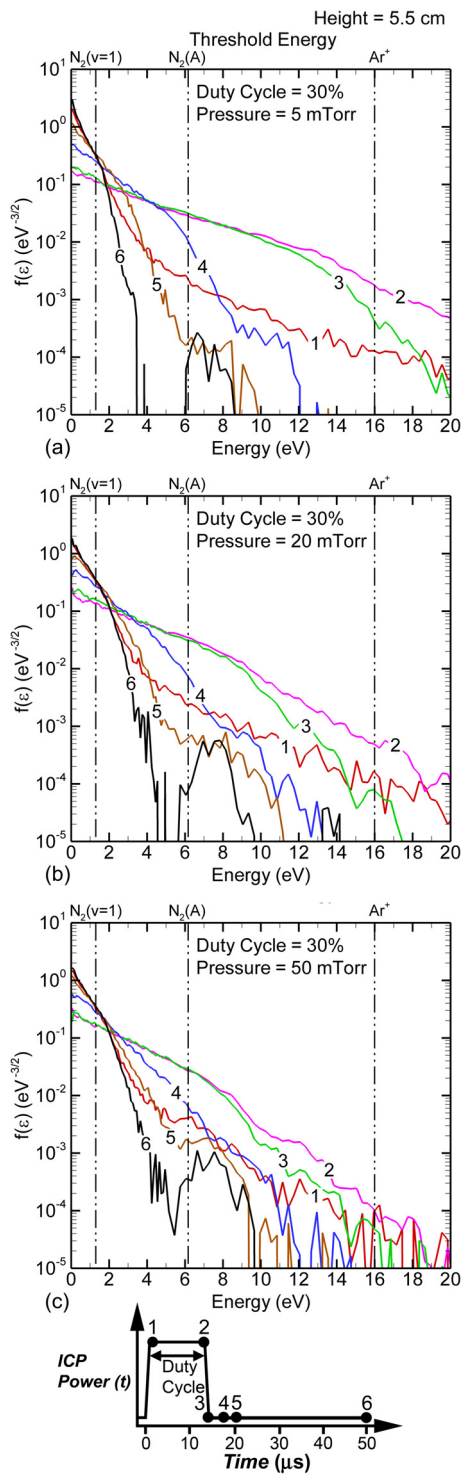


FIG. 11. $f(\varepsilon)$ as a function of time during the pulse period outside the skin depth at a height of 5.5 cm ($\text{Ar}/\text{N}_2 = 80/20$, 300 W pulsed-period-averaged power, 100 sccm, 10 MHz, PRF = 20 kHz, DC = 30%). (a) 5 mTorr. (b) 20 mTorr. (c) 50 mTorr. The threshold energies for $\text{N}_2(v=1)$, $\text{N}_2(\text{A})$, and Ar^+ are shown by the dashed lines.

primarily involves long-mean-free path electrons having energies greater than the plasma potential.

At 20 mTorr and 50 mTorr, the behavior of $f(\varepsilon)$ in the electromagnetic skin depth (Fig. 10) is similar to that at 5 mTorr—an initial extension of the tail of $f(\varepsilon)$, followed by a collisional relaxation. The increase in collisional cooling at 50 mTorr is offset by a decrease in the rate of diffusion

cooling which tends to compensate for each other. Lower in the reactor (Fig. 11), the behavior of $f(\varepsilon)$ is also similar to that at 5 mTorr, except that the tail of $f(\varepsilon)$ during the pulse does not extend to as high an energy. At 5 mTorr, the energy relaxation length, $\lambda_{\varepsilon} \approx 13$ cm, which is essentially the height of the reactor. At 20 mTorr, $\lambda_{\varepsilon} \approx 5.3$ cm, while at 50 mTorr, $\lambda_{\varepsilon} \approx 2.6$ cm. At 5 mTorr, electrons that are heated in the skin depth retain most of their energy convecting to a height of 5.5 cm, a distance of half the energy relaxation length. At 20 mTorr and 50 mTorr, electrons that are heated in the skin depth lose a significant amount of their energy before reaching a height of 5.5 cm, which is over 1 and 2 energy relaxation lengths away for 20 mTorr and 50 mTorr. The tail of $f(\varepsilon)$ therefore fails to extend lower in the reactor at the higher pressures.

The time-averaged EEDs over the pulsed cycle, $\langle f(\varepsilon) \rangle$, as a function of height at a radius of 5.9 cm, for duty cycles of 10%, 30%, and 50% are shown in Fig. 12 for 5 mTorr, and in Fig. 13 for 50 mTorr. The threshold energies for excitation of $\text{N}_2(v=1)$, $\text{N}_2(\text{A})$, and Ar^+ (from the ground state) are noted. At 5 mTorr, the $\langle f(\varepsilon) \rangle$ is not particularly sensitive functions of position and duty cycle except at energies above the threshold energy for excitation of $\text{N}_2(\text{A})$ from the ground state. Above that energy, $\langle f(\varepsilon) \rangle$ for all heights have the same shape but the slope becomes more negative further from the skin depth, a consequence of electron collisions in transit from the skin depth depleting the tail. The $\langle f(\varepsilon) \rangle$ at low duty cycle has a three-temperature distribution, which begins transitioning to a two-temperature distribution as the duty cycle increases. The ranges in energy that correspond to the three temperature regimes are $\varepsilon_1 = 0\text{--}1.0$ eV, $\varepsilon_2 = 1.0\text{--}2.5$ eV, and $\varepsilon_3 > 2.5$ eV. For example, these temperatures are 0.7 eV, 0.6 eV, and 6 eV, at a height of 11.5 cm.

The multi-temperature character of $\langle f(\varepsilon) \rangle$ is a bit deceiving. This shape results from the superposition or average of the individual $f(\varepsilon)$, shown in Figs. 10 and 11, produced at different times during the on and off periods of the pulse. The first two temperature regimes at low energies correspond to the pulse-off period when $f(\varepsilon)$ is thermalizing and is cut-off by the vibrational excitation thresholds. The third regime ($\varepsilon > 2.5$ eV) corresponds to the pulse-on period when the tail of $f(\varepsilon)$ is extended. The large mean free path at 5 mTorr leads to electrons that gain energy in the skin depth of the electric field being able to transit axially through the chamber without losing significant energy. The end result is that the shape of $f(\varepsilon)$ is a weak function of height. That is, electron energy transport is largely non-local.

As the duty cycle decreases, the degree of overshoot in T_e at the start of the pulse increases and the tail of $f(\varepsilon)$ is lifted to a greater degree. This results from two factors. For a given PPA power, a shorter duty cycle means that the peak power during the power-on cycle is larger. Shorter duty cycles produce longer inter-pulse periods, which allows for more recombination and diffusion loss. This produces a smaller electron density at the start of the next power-on cycle which then produces more overshoot. At the same time, a longer duty cycle results in the tail of $f(\varepsilon)$ being elevated for a longer fraction of the period. The end result is a lifting of the tail of $\langle f(\varepsilon) \rangle$ with increasing duty cycle.

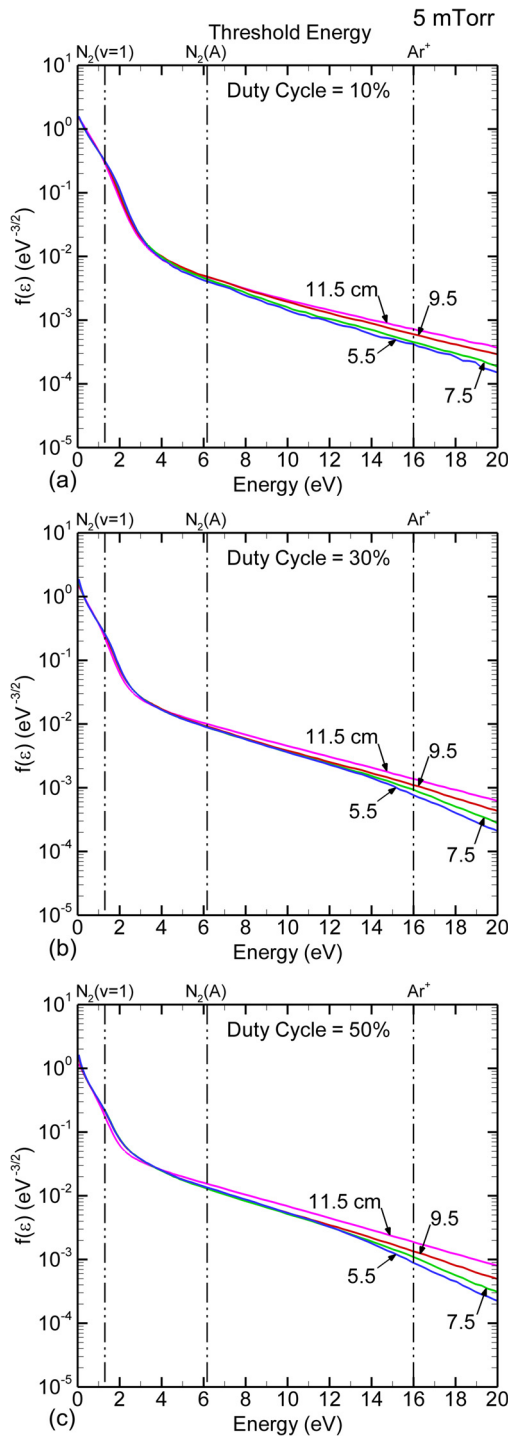


FIG. 12. Pulse averaged $f(\varepsilon)$ at different heights (radius of 5.9 cm) at 5 mTorr for different duty cycles ($\text{Ar}/\text{N}_2 = 80/20$, 300 W pulsed-period-averaged power, 100 sccm, 10 MHz, PRF = 20 kHz). (a) 10%. (b) 30%. (c) 50%. The threshold energies for $\text{N}_2(v=1)$, $\text{N}_2(\text{A})$, and Ar^+ are shown by the dashed lines.

At 50 mTorr, λ_e is significantly reduced which produces a significant height dependence of the tail of $\langle f(\varepsilon) \rangle$ and more clear delineation of the collisional threshold energies, as shown in Fig. 13. There is a more rapid collisional relaxation of the tail of the $f(\varepsilon)$ by electronic excitation of N_2 , beginning with $\text{N}_2(\text{A})$, which produces a more cut-off $\langle f(\varepsilon) \rangle$ with distance from the skin-depth. The general trend of lifting of the

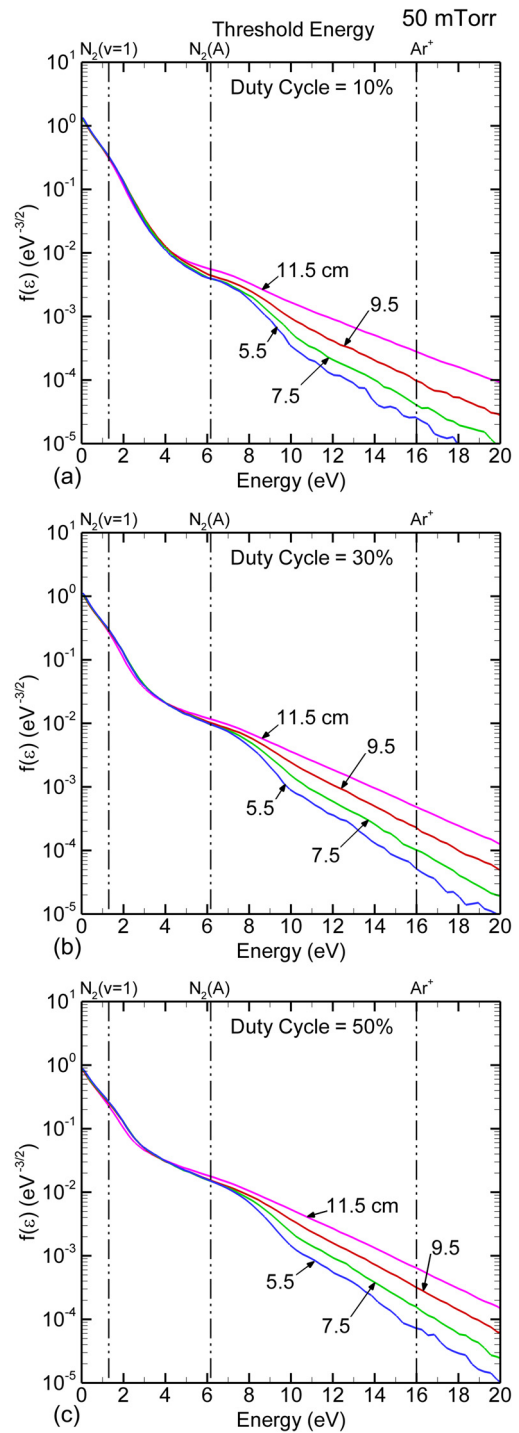


FIG. 13. Pulse averaged $f(\varepsilon)$ at different heights (radius of 5.9 cm) at 50 mTorr for different duty cycles ($\text{Ar}/\text{N}_2 = 80/20$, 300 W pulsed-period-averaged power, 100 sccm, 10 MHz, PRF = 20 kHz). (a) 10%. (b) 30%. (c) 50%. The threshold energies for $\text{N}_2(v=1)$, $\text{N}_2(\text{A})$, and Ar^+ are shown by the dashed lines.

tail of $\langle f(\varepsilon) \rangle$ with increasing duty cycle is, however, similar to that at 5 mTorr.

The spatial profiles for the electron impact source functions for $\text{N}_2(v=1)$ [$S(\text{N}_2(v=1))$], $\text{N}_2(\text{A})$ [$S(\text{N}_2(\text{A}))$], and Ar^+ [$S(\text{Ar}^+)$], at different times during the pulsed cycle are shown in Figs. 14–16. The ICP was operated with a PPA power of 300 W, a duty cycle of 30%, a pressure of 5 mTorr, and a 10 MHz rf frequency. The modulation of the source

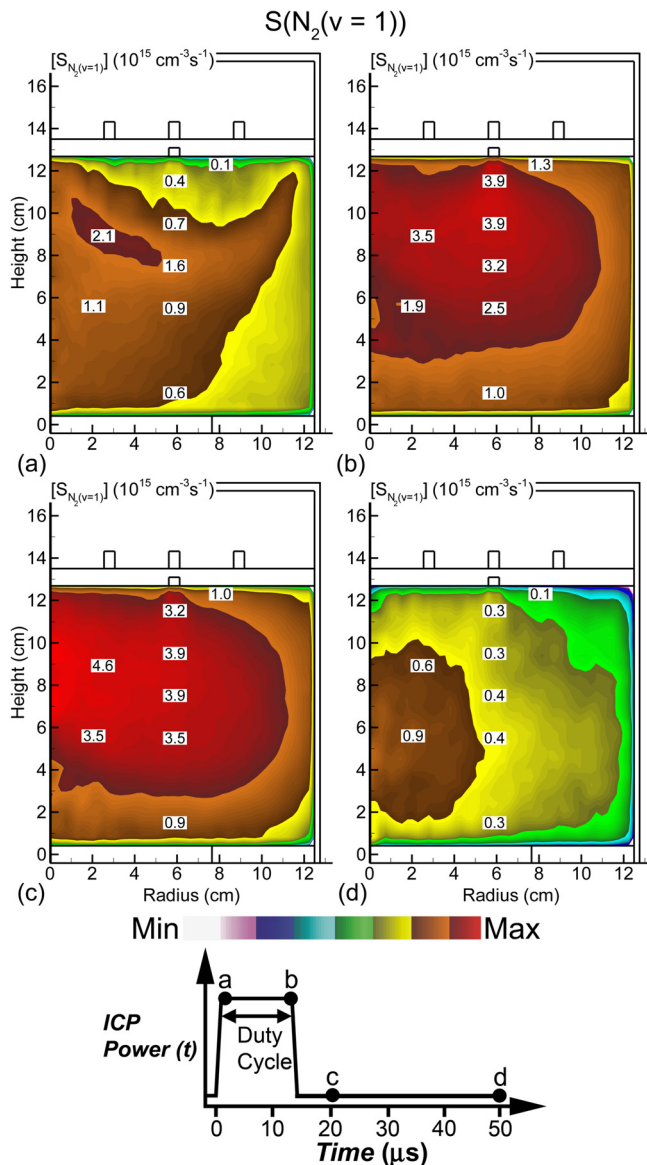


FIG. 14. Electron impact source functions for single step excitation of N_2 ground state to $N_2(v=1)$ at different times during a pulsed cycle indicated by the schematic ($Ar/N_2 = 80/20$, 300 W pulsed-period-averaged power, 100 sccm, 10 MHz, PRF = 20 kHz, 5 mTorr). (a) Start of pulse-on period. (b) End of pulse-on period. (c) 4 μ s after start of afterglow period. (d) End of afterglow period.

function between the pulse-on and pulse-off periods increases as the threshold energy for the process increases. For $N_2(v=1)$, $S(N_2(v=1))$ is significant, 10^{15} – 10^{16} $cm^{-3}s^{-1}$, during the entire pulse-period as the T_e during the pulse-off period of a few tenths of an eV is still sufficient to produce significant vibrational excitation. At the leading edge of the power-on period when T_e overshoots its steady-state value, $S(N_2(v=1))$ is actually depressed in the skin depth for a few cm from the coils. At this time, the extension of the tail of $f(\epsilon)$ depresses the population of electrons 1–3 eV, where the resonant cross section is maximum. The maximum value of $S(N_2(v=1))$ during the pulse period occurs in the early part of the pulse-off period. It is at this time that electrons slowing down from higher energy pass through 1–3 eV range in which the resonant cross sections occur for vibrational excitation.

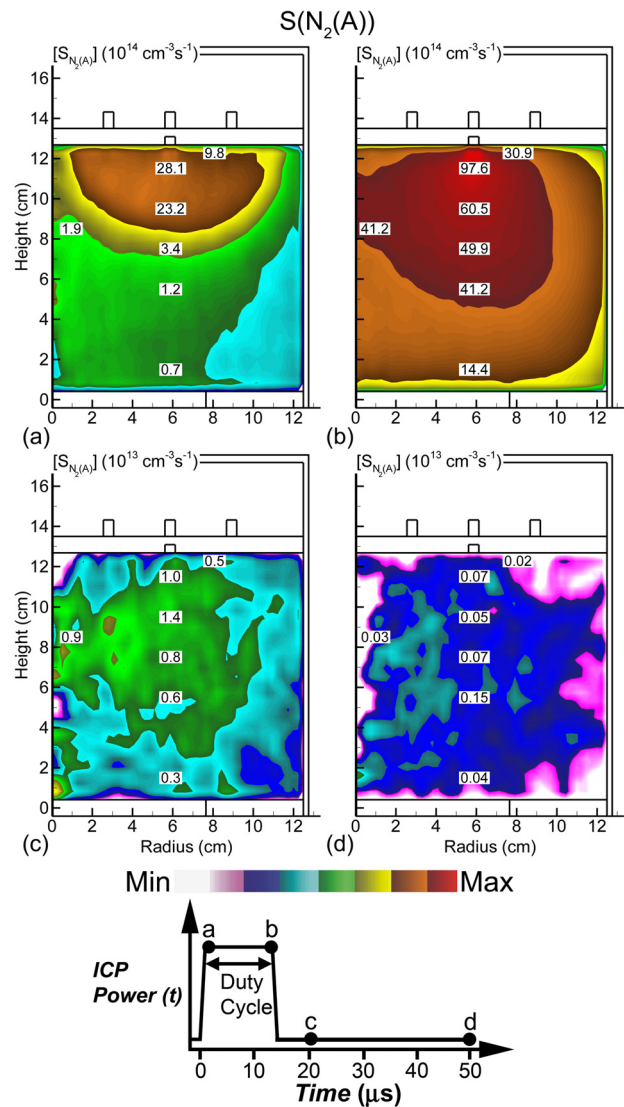


FIG. 15. Electron impact source functions of single step excitation of N_2 to $N_2(A)$ electronic state at different times during a pulsed cycle indicated by the schematic ($Ar/N_2 = 80/20$, 300 W pulsed-period-averaged power, 100 sccm, 10 MHz, PRF = 20 kHz, 5 mTorr). (a) Start of pulse-on period. (b) End of pulse-on period. (c) 4 μ s after start of afterglow period. (d) End of afterglow period.

At the leading edge of the pulse-on period, $S(N_2(A))$ is maximum in the skin depth with a magnitude of 3×10^{15} $cm^{-3}s^{-1}$, and decreases by an order of magnitude at the midplane of the reactor. As the electron density increases and high energy electrons convect out of the skin depth, $S(N_2(A))$ is maximum at the end of the pulse-on period, with a magnitude of 10^{16} $cm^{-3}s^{-1}$, decreasing by only a factor of two at the midplane. Within 5 μ s of the termination of the power, the decay of the tail of $f(\epsilon)$ reduces $S(N_2(A))$ by a factor of 100.

In Ar/N_2 mixtures, there are sources of $N_2(A)$ other than direct electron impact that may compromise the control strategies discussed here based on control of $f(\epsilon)$. For example, metastable and higher excited states of Ar are quenched by N_2 with rate coefficients of about 0.3 – 1.0×10^{-10} cm^3s^{-1} with significant branching to $N_2(A,B,C)$.^{22–24} For a rate coefficient of 10^{-10} cm^3s^{-1} and a unity branching to $N_2(A)$, the

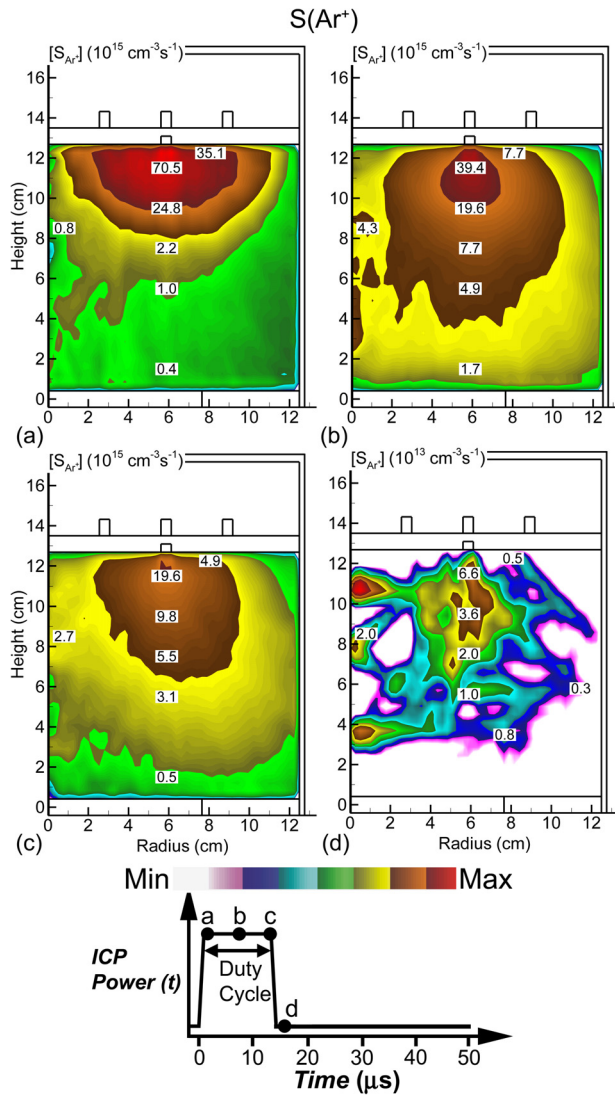


FIG. 16. Electron impact source functions for single step ionization of Ar ground state to Ar^+ at different times during a pulsed cycle indicated by the schematic ($\text{Ar}/\text{N}_2 = 80/20$, 300 W pulsed-period-averaged power, 100 sccm, 10 MHz, PRF = 20 kHz, 5 mTorr). (a) Start of pulse-on period. (b) Middle of pulse-on period. (c) End of pulse-on period. (d) At start of afterglow period (note change in scale).

source of $\text{N}_2(\text{A})$ by excitation transfer is about $2 \times 10^{14} \text{ cm}^{-3} \text{ s}^{-1}$ for the conditions of Fig. 15. This source is smaller by factors of 10–100 than the direct electron impact excitation during the power-on portion of the pulse but the dominant source during the power-off portion of the pulse. Averaged over the pulsed cycle, excitation transfer accounts for about 10% of the formation of $\text{N}_2(\text{A})$.

The modulation of $S(\text{Ar}^+)$ during the pulse period is even more severe. $S(\text{Ar}^+)$ has a maximum value of $7 \times 10^{16} \text{ cm}^{-3} \text{ s}^{-1}$ in the skin depth directly under the center coil corresponding to the overshoot in T_e and raising of the tail of $f(\epsilon)$. As the tail of $f(\epsilon)$ relaxes from its overshoot extension during the power-on period, the maximum of $S(\text{Ar}^+)$ decreases to $2 \times 10^{16} \text{ cm}^{-3} \text{ s}^{-1}$ in spite of there being a 2–3 times increase in electron density. $S(\text{Ar}^+)$, however, becomes more uniform in the reactor as high energy electrons convect further from the skin depth. There is essentially no direct ionization of the ground state within a few

microseconds of the end of the pulsed period as the tail of $f(\epsilon)$ quickly relaxes.

The source functions for $\text{N}_2(v=1)$, $\text{N}_2(\text{A})$, and Ar^+ during different periods of the pulse as a function of duty cycle at a radius of 5.9 cm and height of 11.5 cm, are shown in Fig. 17 for 5 mTorr and Fig. 18 for 50 mTorr. The PPA power is the same for all cases. The general trend is that as the duty cycle decreases, the time-averaged source functions increase. The magnitude of the increase is dependent on the portion of the pulsed cycle the source functions are averaged

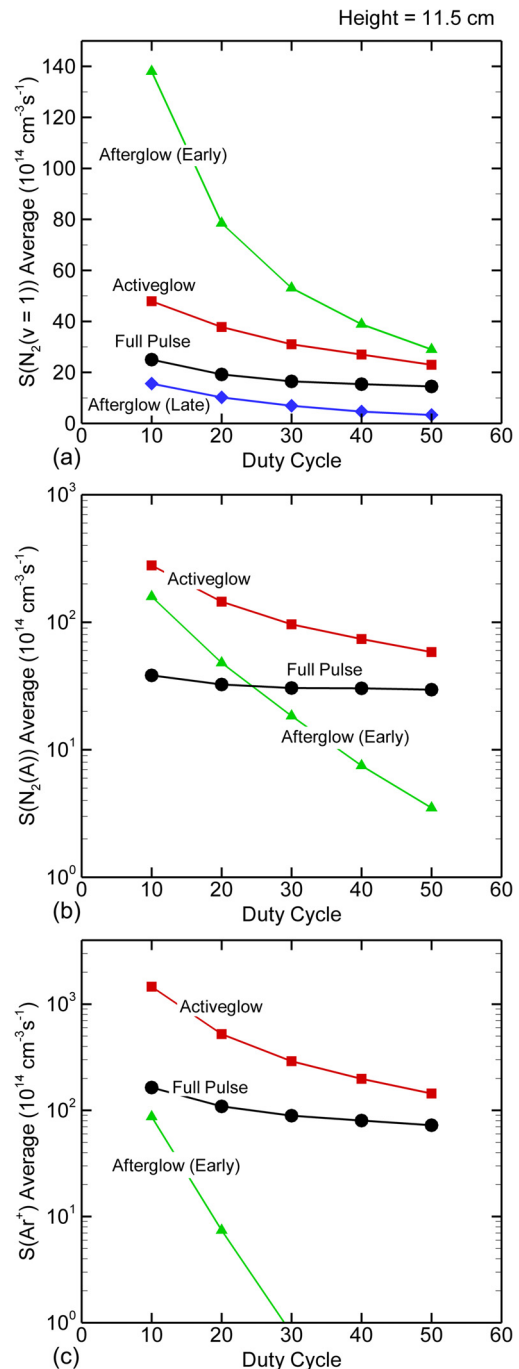


FIG. 17. Pulsed averaged source functions at the edge of the skin-depth (height = 11.5 cm) for 5 mTorr during different time periods in the pulse as a function of duty cycle ($\text{Ar}/\text{N}_2 = 80/20$, 300 W pulsed-period-averaged power, 100 sccm, 10 MHz, PRF = 20 kHz). Sources are for single step production of (a) $\text{N}_2(v=1)$. (b) $\text{N}_2(\text{A})$ electronic state. (c) Ar^+ .

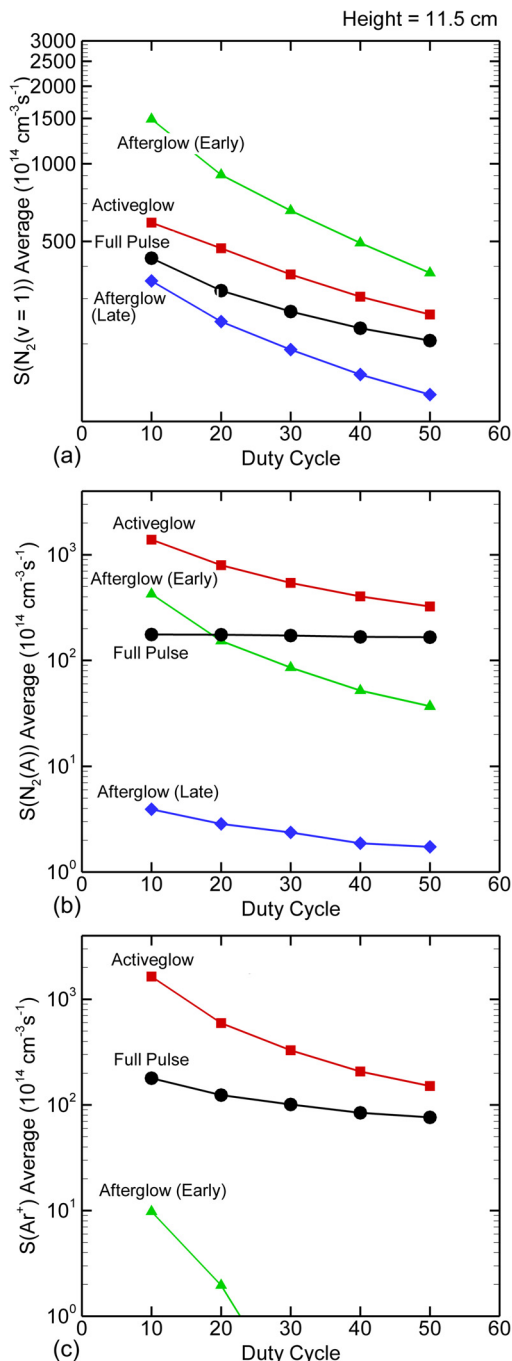


FIG. 18. Pulsed averaged source functions at the edge of the skin-depth (height = 11.5 cm) for 50 mTorr during different time periods in the pulse as a function of duty cycle (Ar/N₂ = 80/20, 300 W pulsed-period-averaged power, 100 sccm, 10 MHz, PRF = 20 kHz). Sources are for single step production of (a) N₂(v = 1). (b) N₂(A) electronic state. (c) Ar⁺.

over. The duty cycle, however, has little effect on the magnitude of the source functions averaged over the entire pulse period. At most, cycle averaged source functions change by a factor of two between a 10% to 50% duty cycle.

In general, the PPA source function increases with decreasing duty cycle regardless of whether averaging over the full pulse period or a subset of the full period. The largest increase in S(N₂(v = 1)) with decreasing duty cycle occurs in the early afterglow and this is also when the maximum value of S(N₂(v = 1)) occurs. For S(N₂(A)) and S(Ar⁺), the

greatest fractional increase also occurs in the early afterglow, but the maximum values occur in the activeglow. For the high threshold energy processes, the source functions are negligible in the late afterglow. As the duty cycle decreases with the PPA power remaining constant, a higher peak power is deposited into the plasma during the pulse-on period. This leads to a higher T_e and a higher rate of ionization during the pulse. The source functions for high threshold energy processes increase in the early afterglow with decreasing duty cycle. This trend is in large part due to the finite rate of thermalization of T_e from its value during the activeglow which, for shorter duty cycles, provides significant excitation even after the power has been terminated.

Increasing pressure from 5 mTorr to 50 mTorr increases S(N₂(v = 1)) by a factor of ≈ 11 –13 for the activeglow and early afterglow periods, ≈ 22 –38 for the late afterglow period, and ≈ 14 –17 for the full pulse period depending on duty cycle. Increasing gas pressure not only increases the gas density but also increases the electron density. For S(N₂(v = 1)) which is not terribly sensitive to T_e , these increases gas and electron density produce an increase in S(N₂(v = 1)).

At 50 mTorr, S(N₂(v = 1)) and S(Ar⁺), averaged over the full pulse period, do not significantly change as a function of duty cycle. Even though the magnitude of the source functions for the active glow and early afterglow increase with decreasing duty cycle, this increase occurs over a shorter time. The magnitudes of the source functions in the late afterglow are three orders of magnitude smaller than in the activeglow, so little contribution is made to the time average. The end result is that the integral is nearly constant.

Source functions were also investigated for a PPA power of 75 W, pressures of 5 and 50 mTorr, and duty cycles of 10%, 30%, and 50%. With the exception of magnitudes of source functions that are larger at the higher power, the trends discussed here are essentially the same. The exception is that there is increased modulation in the source functions of N₂(v = 1) and N₂(A) over the pulse at 5 mTorr. The increase modulation is a result of a larger reduction of the source functions in the afterglow compared to the activeglow. The higher power produces a larger population of excited states which then sustain T_e through superelastic collisions in the afterglow.

Even though at 5 mTorr, the time-averaged S(Ar⁺) over the entire pulse can be larger than S(N₂(v = 1)), Ar⁺ is almost exclusively generated during the pulse-on period, while N₂(v = 1) is generated throughout the pulse. The ratio of S(Ar⁺) to S(N₂(v = 1)), and so their fluxes to surfaces, can then significantly vary during the pulsed cycle. For example, if a surface chemistry process depends only on the separate fluences of ions or excited states, then duty cycle is not a critical variable. However, if the process depends on the ratio of ion fluxes to excited state fluxes, then duty cycle may be a sensitive control variable to vary this ratio.

V. CONCLUDING REMARKS

Results from a computational investigation of the potential of using pulsed ICPs to control $f(\epsilon)$ of electrons

and the magnitude of the source functions for low, mid, and high threshold energy processes were discussed. The source functions for $N_2(v=1)$, $N_2(A)$, and Ar^+ are used to represent low, mid, and high threshold energy processes, respectively. We found that duty cycle does not have a significant impact on the *time-averaged values* over the full pulse, of either $f(\varepsilon)$ or the source functions. There is, however, significant modulation during the pulse cycle. We found that the multi-temperature shapes of pulse averaged $\langle f(\varepsilon) \rangle$ result from the superposition of a highly extended tail of $f(\varepsilon)$ during the active glow (producing the tail temperature) and a thermalizing $f(\varepsilon)$ during the afterglow (producing the bulk temperature). These modulations then produce differences in the ratios of source functions during the pulse cycle which are in turn functions of duty cycle. Pressure has a significant effect on both $f(\varepsilon)$ and source functions. Increasing pressure produces a shorter electron energy relaxation distance, λ_e , and higher electron densities during the pulse, which reduces the skin depth of the electromagnetic wave. All of this lead to a lowering of the tail of $f(\varepsilon)$, particularly outside of the skin depth, as well as a more significant dependence of $f(\varepsilon)$ on height in the reactor. PPA power has little effect on the overall shape of $f(\varepsilon)$ except to lower the tail of $f(\varepsilon)$ in the afterglow at lower power. This is due to the decrease in superelastic heating of $f(\varepsilon)$ by the lower density of excited states and a lower rate of e-e collisions which tend to populate the tail of $f(\varepsilon)$.

ACKNOWLEDGMENTS

This work was supported by the Semiconductor Research Corporation, the National Science Foundation

(CHE-1124724) and the Department of Energy Office of Fusion Energy Science (DE-SC0001319).

- ¹D. J. Economou, *Thin Solid Films* **365**, 348 (2000).
- ²S. Banna, A. Agarwal, G. Cunge, M. Darnon, E. Pargon, and O. Joubert, *J. Vac. Sci. Technol. A* **30**, 040801 (2012).
- ³C. Cardinaud, M.-C. Peignon, and P.-Y. Tessier, *Appl. Surf. Sci.* **164**, 72 (2000).
- ⁴D. J. Economou, *J. Phys. D: Appl. Phys.* **47**, 303001 (2014).
- ⁵K. Takahashi, M. Hori, and T. Goto, *Jpn. J. Appl. Phys. Part 1* **32**, 1088 (1993).
- ⁶T. Goto and M. Hori, *Jpn. J. Appl. Phys. Part 1* **35**, 6521 (1996).
- ⁷Y. Yasaka and K. Nishimura, *Plasma Sources Sci. Technol.* **7**, 323 (1998).
- ⁸M. Bauer, T. Schwarz-Selinger, H. Kang, and A. von Keudell, *Plasma Sources Sci. Technol.* **14**, 543 (2005).
- ⁹P. Bodart, M. Brihoum, G. Cunge, O. Joubert, and N. Sadeghi, *J. Appl. Phys.* **110**, 113302 (2011).
- ¹⁰G. Cunge, P. Bodart, M. Brihoum, F. Boulard, T. Chevolleau, and N. Sadeghi, *Plasma Sources Sci. Technol.* **21**, 024006 (2012).
- ¹¹U. Kortshagen, I. Pukropski, and M. Zethoff, *J. Appl. Phys.* **76**, 2048 (1994).
- ¹²H. Singh and D. B. Graves, *J. Appl. Phys.* **87**, 4098 (2000).
- ¹³M. V. Malyshev and V. M. Donnelly, *Plasma Sources Sci. Technol.* **9**, 353 (2000).
- ¹⁴G. A. Hebner and C. B. Fleddermann, *J. Appl. Phys.* **82**, 2814 (1997).
- ¹⁵T. Kimura and K. Ohe, *J. Appl. Phys.* **89**, 4240 (2001).
- ¹⁶A. Maresca, K. Orlov, and U. Kortshagen, *Phys. Rev. E* **65**, 056405 (2002).
- ¹⁷V. A. Godyak, R. B. Piejak, and B. M. Alexandrovich, *Plasma Sources Sci. Technol.* **11**, 525 (2002).
- ¹⁸V. A. Godyak, "Nonequilibrium EEDF in gas discharge plasmas," *IEEE Trans. Plasma Sci.* **34**, 755 (2006).
- ¹⁹M. J. Kushner, *J. Phys. D: Appl. Phys.* **42**, 194013 (2009).
- ²⁰S.-H. Song and M. J. Kushner, *Plasma Sources Sci. Technol.* **21**, 055028 (2012).
- ²¹T. Kimura and H. Kasugai, *J. Appl. Phys.* **108**, 033305 (2010).
- ²²N. Sadeghi, D. W. Setser, A. Francis, U. Czarnetzki, and H. F. Dobeles, *J. Chem. Phys.* **115**, 3144 (2001).
- ²³W. Van Gaens and A. Bogaerts, *J. Phys. D: Appl. Phys.* **46**, 275201 (2013).
- ²⁴M. Bourene and J. Le Calve, *J. Chem. Phys.* **58**, 1452 (1973).